

# CLASH: EXTREME EMISSION LINE GALAXIES AND THEIR IMPLICATION ON SELECTION OF HIGH-REDSHIFT GALAXIES

XINGXING HUANG<sup>1,2</sup>, WEI ZHENG<sup>2</sup>, JUNXIAN WANG<sup>1</sup>, HOLLAND FORD<sup>2</sup>, DORON LEMZE<sup>2</sup>, JOHN MOUSTAKAS<sup>3</sup>, XINWEN SHU<sup>4,1</sup>, ARJEN VAN DER WEL<sup>5</sup>, ADI ZITRIN<sup>6,7</sup>, BRENDA L. FRYE<sup>8</sup>, MARC POSTMAN<sup>9</sup>, MATTHIAS BARTELMANN<sup>10</sup>, NARCISO BENÍTEZ<sup>11</sup>, LARRY BRADLEY<sup>9</sup>, TOM BROADHURST<sup>12,13</sup>, DAN COE<sup>9</sup>, MEGAN DONAHUE<sup>14</sup>, LEOPOLDO INFANTE<sup>15</sup>, DANIEL KELSON<sup>16</sup>, ANTON KOEKEMOER<sup>9</sup>, OFER LAHAV<sup>17</sup>, ELINOR MEDEZINSKI<sup>2</sup>, LEONIDAS MOUSTAKAS<sup>16</sup>, PIERO ROSATI<sup>19</sup>, STELLA SEITZ<sup>20</sup>, KEIICHI UMETSU<sup>21</sup>

*Draft version August 20, 2018*

## ABSTRACT

We utilize the CLASH (Cluster Lensing And Supernova survey with Hubble) observations of 25 clusters to search for extreme emission-line galaxies (EELGs). The selections are carried out in two central bands: F105W ( $Y_{105}$ ) and F125W ( $J_{125}$ ), as the flux of the central bands could be enhanced by the presence of [O III]  $\lambda\lambda 4959, 5007$  at redshift of  $\sim 0.93 - 1.14$  and  $1.57 - 1.79$ , respectively. The multi-band observations help to constrain the equivalent widths of emission lines. Thanks to cluster lensing, we are able to identify 52 candidates down to an intrinsic limiting magnitude of 28.5 and to a rest-frame [O III]  $\lambda\lambda 4959, 5007$  equivalent width of  $\simeq 3737$  Å. Our samples include a number of EELGs at lower luminosities that are missed in other surveys, and the extremely high equivalent width can be only found in such faint galaxies. These EELGs can mimic the dropout feature similar to that of high redshift galaxies and contaminate the color-color selection of high redshift galaxies when the S/N ratio is limited or the band coverage is incomplete. We predict that the fraction of EELGs in the future high redshift galaxy selections cannot be neglected.

**Keywords:** galaxies: high-redshift–galaxies: formation–galaxies: photometry

## 1. INTRODUCTION

The presence of extremely strong emission lines such as the [O III]  $\lambda\lambda 4959, 5007$  and H $\alpha$   $\lambda 6563$  emission lines is one of the prominent spectral features in star-forming galaxies. Recently, a considerable number of star-forming galaxies with extraordinarily strong [O III]  $\lambda\lambda 4959, 5007$  (Straughn et al. 2009; van der Wel et al. 2011; Atek et al. 2011; Smit et al. 2014) or H $\alpha$   $\lambda 6563$  (Shim et al. 2011; Shim & Chary 2013) lines have been found. While some of these galaxies are identified spectroscopically (Erb et al. 2006; Atek et al. 2011; Frye et al. 2012), the majority of them are found from broad-band photometry with a significant flux excess in one or more bands. Utilizing *HST*/Wide Field Camera 3 (WFC3) observations of the Cosmic Assembly Near-IR Deep Extragalactic Legacy Survey (CANDELS, Grogin et al. 2011), van der Wel et al. 2011 (VDW11 hereafter) identified an abundant population of extreme emission line galaxies (EELGs) at redshift  $z \sim 1.7$ . In some cases, the rest-frame equivalent widths (EWs) of such strong emission lines reach 2000 Å or even higher.

Extremely strong emission lines can affect the spectral-energy-distribution (SED) fitting of broad-band photometry (Schaerer & de Barros 2009; Atek et al. 2011; Shim et al. 2011; Labbé et al. 2010, 2012; Stark et al. 2013; Fumagalli et al. 2012). Their contributions may mimic the spectral feature of the Lyman break in high-redshift galaxies. It is therefore possible that some high-redshift Lyman break galaxies (LBG) may actually be low-redshift EELGs when the wavelength coverages or depths are limited. Recently, the search for LBG has reached  $z > 9$ , and *HST* plays the major role in this redshift range with the WFC3/IR instrument (Bouwens et al. 2011; Zheng et al. 2012; Coe et al. 2013; Ellis

<sup>1</sup> CAS Key Laboratory for Research in Galaxies and Cosmology, Department of Astronomy, University of Science and Technology of China, Hefei, Anhui 230026, China; e-mail:hxx@mail.ustc.edu.cn

<sup>2</sup> Department of Physics and Astronomy, Johns Hopkins University, 3400 N. Charles Street, Baltimore, MD 21218

<sup>3</sup> Department of Physics & Astronomy, Siena College, 515 Loudon Road, Loudonville, NY, 12211, USA

<sup>4</sup> CEA Saclay, DSM/Irfu/Service d'Astrophysique, Orme des Merisiers, 91191 Gif-sur-Yvette Cedex, France

<sup>5</sup> Max-Planck Institute for Astronomy, Königstuhl 17, D-69117, Heidelberg, Germany

<sup>6</sup> Cahill Center for Astronomy and Astrophysics, California Institute of Technology, MS 249-17, Pasadena, CA 91125

<sup>7</sup> Hubble Fellow

<sup>8</sup> Steward Observatory/Department of Astronomy, University of Arizona, 933 N Cherry Ave, Tucson, AZ 85721-0065

<sup>9</sup> Space Telescope Science Institute, 3700 San Martin Drive, Baltimore, MD 21208, U.S.A.

<sup>10</sup> Leiden Observatory, Leiden University, P. O. Box 9513, 2300 RA Leiden, The Netherlands

<sup>11</sup> Instituto de Astrofísica de Andalucía (CSIC), C/Camino Bajo de Huétor 24, Granada 18008, Spain

<sup>12</sup> Department of Theoretical Physics, University of Basque Country UPV/EHU, Bilbao, Spain

<sup>13</sup> IKERBASQUE, Basque Foundation for Science, Bilbao, Spain

<sup>14</sup> Department of Physics and Astronomy, Michigan State University, East Lansing, MI 48824, USA

<sup>15</sup> Departamento de Astronomía y Astrofísica, Pontificia Universidad Católica de Chile, V. Mackenna 4860, Santiago 22, Chile

<sup>16</sup> Observatories of the Carnegie Institution of Washington, Pasadena, CA 91 101, USA

<sup>17</sup> Department of Physics and Astronomy, University College London, Gower Street, London WC1E 6 BT, UK

<sup>18</sup> Center for Astrophysics and Space Sciences, University of California at San Diego, 9500 Gilman Dr., MC 0424, La Jolla, CA 92093, USA

<sup>19</sup> Institute of Astronomy and Astrophysics, Academia Sinica, P. O. Box 23-141, Taipei 10617, Taiwan

<sup>20</sup> Universitäts-Sternwarte, München, Scheinerstr. 1, D-81679 München, Germany

<sup>21</sup> Institut für Theoretische Astrophysik, ZAH, Albert-Ueberle-Straße 2, 69120 Heidelberg, Germany

et al. 2013; Oesch et al. 2013). UDFj-39546284 was first detected in the Hubble Ultra Deep Field (HDF09) with an  $H_{160}$  band detection only (Bouwens et al. 2011). The decrement between the F160W and F125W bands is larger than two magnitudes, thus suggestive of a  $z \simeq 10$  candidate. Followup observations of the HUDF12 (GO 12498: PI Ellis) and CANDELS program (Grogin et al. 2011) confirm that this substantial break in the SED is actually between the F160W and F140W bands (Ellis et al. 2013; Bouwens et al. 2013a), implying an even higher redshift. Brammer et al. (2013) analyzed deep WFC3 grism observations of UDFj-39546284 and found a  $2.7\sigma$  detection of an emission line at  $1.599 \mu\text{m}$ . In the deep Keck observation, Capak et al. (2013) also found a  $2.2\sigma$  peak at the same wavelength. Both spectra suggest that UDFj-39546284 could be a strong [O III]  $\lambda 5007$  emitter at  $z \sim 2.19$  or a strong [O II]  $\lambda 3727$  emitter at  $z \sim 3.29$ . Current deep near infrared observations are unlikely to determine the nature of this candidate. The presence of UDFj-39546284 suggests that the possible contamination due to EELGs at lower redshift should be reexamined.

In this paper, we report the search for EELGs at two redshift ranges in the CLASH cluster fields to estimate the contamination to the selections of LBG. The CLASH program (Postman et al. 2012) is a 16-band survey of 25 clusters between 0.2 and  $1.6 \mu\text{m}$ . The nominal limiting magnitude in the F160W band is approximately 27.2 ( $5\sigma$  detection limit). With the power of cluster lensing, some of target can reach an intrinsic AB magnitude  $\sim 29$  mag, similar to that of  $z \sim 10$  galaxies in the Hubble Ultra Deep Field.

Throughout this paper, EW is referred to the total of [O III]  $\lambda\lambda 4959, 5007$  and  $H\beta$   $\lambda 4861$  in the rest frame unless specified otherwise. Magnitudes are calculated in the AB system. Errors are computed at  $1\sigma$ . We adopt a flat cosmology with  $\Omega_\Lambda = 0.7$ ,  $\Omega_M = 0.3$  and  $H_0 = 70 \text{ km s}^{-1} \text{ Mpc}^{-1}$ .

## 2. DATA

### 2.1. Data Reduction

The CLASH data were obtained with three *HST* cameras: ACS (Advanced Camera for Surveys)/WFC, WFC3 (Wide Field Camera 3)/IR and WFC3/UVIS. All the 25 clusters have now been observed. The images and catalogs are processed with APLUS (Zheng et al. 2012a), which is an automatic pipeline modified from the APSIS package (Blakeslee et al. 2003) with an enhanced capability of processing WFC3 data and aligning them with the ACS data. APLUS processes the calibrated images from the *HST* instrument pipelines, namely the *flt* images for ACS (corrected for the detector’s charge transfer efficiency) and *flt* images for WFC3/IR. Recently, APLUS has been updated so that images of individual exposure are aligned using *DrizzlePac* (Gonzaga et al. 2012), and the accuracy can achieve  $1/5$  pixel ( $\sim 0''.015$ ) or better.

In the APLUS process, images of different filter bands and cameras were further aligned, resampled and combined with a common pixel scale of  $0.065''$ . We created detection images from the weighted sum of ACS/WFC and WFC3/IR images and ran SExtractor (Bertin & Arnouts 1996) in a dual mode for all 16 bands. *mag-iso* were chosen in the color selections. We also verified

the photometry by comparing with public catalogs,<sup>22</sup> which were processed with modified version of the *Mosaicdrizzle* pipeline (Koekemoer et al. 2003, 2011), and no systematic deviation was found between the two pipelines. In this paper, we focus on two ACS/WFC filters (F814W, F850lp) and five WFC3/IR filters (F105W, F110W, F125W, F140W, F160W), which are hereafter called  $I_{814}$ ,  $Z_{850}$ ,  $Y_{105}$ ,  $Y_{J110}$ ,  $J_{125}$ ,  $JH_{140}$ , and  $H_{160}$  bands.

### 2.2. Sample Selection

A color-color selection has been successfully used for identifying EELGs in VDW11. We carried out two selections with two sets of filter bands. Firstly, we follow the selection criteria of VDW11, namely

$$J_{125} - I_{814} < -0.44 - \sigma \wedge J_{125} - H_{160} < -0.44 - \sigma$$

In the other selection, we use the  $Y_{105}$  band as the central band, namely

$$Y_{105} - I_{814} < -0.44 - \sigma \wedge Y_{105} - H_{160} < -0.44 - \sigma$$

Where the  $\sigma$  refers to the  $1\sigma$  error of the color. We also require that the three bands in each selection are detected at least  $3\sigma$  to ensure good EW measurements. After these preliminary selections (Figure 1), we check the images and photometry of the WFC3/IR bands for each object. Sources contaminated by cosmic-ray events, nearby bright sources and detector-edge effects are excluded. We build two samples with 40 and 12 candidates named as the “J” sample and “Y” sample. Note that the color excess of 0.44 magnitude in  $J_{125}$  and  $Y_{105}$  corresponds to rest-frame EW of about  $600 \text{ \AA}$ . The false-color images of these galaxies are shown in Figure 2. We include the apparent angular sizes which are measured through full width at half maximum (FWHM) by SExtractor in Table 1 and Table 2.

### 2.3. Redshift Estimation

To illustrate the boosting effect in different bands and different redshifts, we simulate model spectra with a simple power-law continuum plus emission lines and obtain the observed magnitudes using the throughputs of *HST* filters (lower panel in Figure 3). The index of the power-law continuum is fixed at  $\beta = 2$ , which is defined as  $F_\lambda \sim \lambda^{-\beta}$ . Such continuum is a constant in different wavelength with AB magnitude system, and is set to 28 mag. In the model, we choose metal-line lists from galaxies with sub-solar metallicity of  $Z = 0.2Z_\odot = 0.004$  in Anders & Fritze-v. Alvensleben (2003) and only include emission lines with relative line intensities  $F_{line}/F_{H\beta}$  larger than 0.1. The  $H_\alpha$  line is included by assuming the ratio  $H_\alpha/H_\beta = 2.86$  from case B recombination (Storey & Hummer 1995).

In the model, the EW([O III]  $\lambda 5007$ ) is set to  $2000 \text{ \AA}$ . The simulated magnitudes and colors are shown with thick blue lines in Figure 4. Based on this model, those EELGs in the redshift ranges  $\sim 1.57 - 1.79$  (the J sample) and  $\sim 0.93 - 1.14$  (the Y sample) are selected (grey regions in Figure 4). The redshift ranges would not change significantly if we use a different EW in the model. The upper panel of Figure 3 shows the wavelength ranges

<sup>22</sup> <http://archive.stsci.edu/prepds/clash/>

where the strongest emission lines,  $H\alpha$   $\lambda 6563$ ,  $[\text{O III}]$   $\lambda 5007$ ,  $[\text{O II}]$   $\lambda 3727$  impact the observed flux. For the Y sample, the  $[\text{O II}]$   $\lambda 3727$  falls into the  $I_{814}$  band, thus EELGs with stronger emission lines can be selected.

The spectral slopes of star-forming galaxies have been shown with a  $1\sigma$  dispersion of 0.4 (Bouwens et al. 2009). In the second model, we take into consideration the effect of spectral slopes and vary them between  $\beta = 1.5$  and 2.5. The effect is shown in a blue shadow region in the right panel of Figure 4. The changes in spectral slope would affect the color excess lower than 0.25 magnitude. Some EELGs with blue slopes will not be selected. However, as the continuum is calculated with the average of the two bands at different wavelengths, the change of slope is not a problem in the following EW estimates.

Other emission lines, especially  $H\alpha$   $\lambda 6563$  and  $[\text{O II}]$   $\lambda 3727$ , may also contribute to the broad-band photometry, but the relative flux to  $[\text{O III}]$   $\lambda 5007$  will vary due to the difference in metallicity, star formation history and extinction (Anders & Fritze-v. Alvensleben 2003; Kewley et al. 2004; Salzer et al. 2005). In order to show the boosting effect, we build a model with line intensities from metallicity  $Z = 0.02Z_{\odot}$  galaxy (green dots in Figure 4). In another model, we remove all other emission lines to show the contribution of  $[\text{O III}]$   $\lambda\lambda 4959, 5007$  only (red lines in Figure 4). While most emission lines do not affect the photometry as significantly as  $[\text{O III}]$   $\lambda\lambda 4959, 5007$ ,  $H\alpha$   $\lambda 6563$  also boosts the magnitudes as its strength is similar to  $[\text{O III}]$  in typical star-forming galaxies and the  $[\text{O II}]$   $\lambda 3727$  cannot be ignored.

As shown with the red lines in Figure 4, EELGs with redshift 1.14–1.57 would also be selected into the Y sample or J sample, only if  $H\alpha$   $\lambda 6563$  is extremely weak. The  $[\text{O III}]$   $\lambda 5007$  lines can be excited by massive stars as well as active galactic nuclei (AGN). The relatively strong  $[\text{O III}]$   $\lambda 5007$  and weak  $H\alpha$   $\lambda 6563$  can be due to either metal-poor star-forming galaxies or the contribution of AGN (Kauffmann et al. 2003). To exclude these EELGs from the J sample is not possible with current observations. In the Y sample, these EELGs can be identifiable by comparing the magnitudes of  $JH_{140}$  and  $H_{160}$ . As the  $H\alpha$   $\lambda 6563$  falls in both the two bands in these galaxies, the two bands should be observed with similar magnitudes as shown in the left of Figure 4. We find 5/12 candidates in the Y sample have similar  $JH_{140}$  and  $H_{160}$  magnitudes. If parts of these weak  $H\alpha$  EELGs with low  $H\alpha/[\text{O III}]$  ratios are AGN, the upper limit of the AGN fraction in our Y sample is about 42% (5/12), which is still consistent with the AGN fraction ( $\sim 17\%$ ) estimated with a larger spectral emission line galaxy sample in Atek et al. (2011). As our analysis is not sensitive to the redshift, we assume that the redshift ranges are  $z \sim 1.57 - 1.79$  and  $0.93 - 1.14$  for the J and Y samples, respectively.

#### 2.4. Magnification

The major advantage of CLASH observations is that cluster lensing provides a powerful tool to enable us to discover intrinsically faint galaxies. The magnification maps for all 25 clusters are made based on the strong lensing model of Zitrin et al. (2009, 2011). As magnification factors are redshift dependent, we use the median redshift 1.03 for the Y sample and 1.68 for the J samples in calculations. However, the following EW calculations

are based on the color excesses, and thus independent of magnifications. The uncertainties of magnifications are lower than 10% for the ranges of redshifts. The estimated magnifications are likely in consistent with the true value at 68% confidence for magnifications lower than 5 (Figure 11 in Bradley et al. 2013). The uncertainties are only significant for those high magnified candidates.

The source magnification factors are listed in Table 1 and 2. Candidate J22 has a magnification as large as 8.4 and shows an apparent extended structure. The delensed magnitude is estimated as  $\sim 28$  mag. Its EW is higher than 2000 Å, as confirmed with the color excess in  $YJ_{110}$ ,  $J_{125}$ , and  $JH_{140}$ . The magnification distributions of our two samples are shown in Figure 5 in red color. We also calculate the magnifications for field galaxies that are within the same two redshift ranges as our samples in all 25 clusters, and show the distributions in filled blue histograms.

### 3. EW ESTIMATES

Due to the lack of deep near-infrared spectroscopic data for our samples, we estimate the EWs by comparing the flux excess between the bands boosted by the strong emission lines (the central peak bands) and the adjacent bands dominated by the continuum (the continuum bands). As shown in Figure 3 and 4, the strong emission lines boost more than two bands, thus the combination of EWs estimated from different boosted bands makes the EW more reliable.

#### 3.1. Method

The EW is estimated using two continuum bands and one central peak band through:

$$EW = \frac{F_{\text{total}} - F_c}{F_c} \frac{W}{1+z} \quad (1)$$

where  $F_{\text{total}}$  is the flux of the central peak band which is the total flux of emission lines and continuum, and  $F_c$  is the continuum flux in the  $I_{814}$  and  $H_{160}$  bands.  $W$  is the effective width of the central peak bands.  $z$  is the redshift of the EELGs and is set to the median redshifts, which are 1.03 and 1.68 for the Y and J samples, to translate EW to the rest frame. An accurate continuum analysis is important to estimate the EW. In the procedure, we assume the spectral slopes equal 2 to estimate the continuum based on the  $I_{814}$  and  $H_{160}$  bands, and use the weighted averages as the continuum at the central peak bands. In the redshifts of our two samples, the rest frame UV continuum are observed by ACS/WFC bands, thus the UV slopes can be obtained by linear fits of these bands (Column 11 in Table 1 and Table 2). The average slopes of the J and Y samples are  $2.06 \pm 0.02$  and  $2.07 \pm 0.03$ , consistent with our assumption and other studies of strong emission line galaxies (van der Wel et al. 2011, 2013).

The uncertainties in the EW measurement is because that other emission lines could affect the  $I_{814}$  and  $H_{160}$  photometry and cause an overestimate of the continuum level and subsequently an underestimate of the EW. Within our model of  $EW = 2000\text{\AA}$ , the continuum is boosted by less than 0.1 mag for the J sample but larger for the Y sample, in which the  $[\text{O II}]$   $\lambda 3727$  line falls into the  $I_{814}$  bands. Therefore, the EW should be considered as a lower limit in this situation. Furthermore, the



continuum bands are considerably fainter than the center peak bands. Even if the continuum flux is estimated by averaging two continuum bands, the continuum errors are still the main affecting factors of the EW measurements. For some faint EELGs, their continuum flux cannot be well constrained by photometric data due to these facts, which limit the accuracy of EW calculations.

As shown in Figure 3 and 4, all the  $YJ_{110}$ ,  $J_{125}$ ,  $JH_{140}$  are covered by the  $[\text{OIII}]+H_{\beta}$  for the J sample, thus the EWs can be constrained from the color excesses of these three bands. Then the measurements can be verified by comparing EWs calculated from different center peak bands (Figure 6). The uncertainties in EW measurements are slightly higher for broader bands such as  $YJ_{110}$ . Nonetheless, the consistency of EWs inferred from three broad bands makes our results robust.

At the redshift of the Y sample (Figure 4),  $H\alpha$   $\lambda 6563$  has moved into the wavelength ranges of  $J_{125}$  and  $JH_{140}$ , both  $[\text{OIII}]+H_{\beta}$  and  $H\alpha$   $\lambda 6563$  are covered by the  $YJ_{110}$ . The  $Y_{105}$  band is boosted by  $[\text{OIII}]+H_{\beta}$  only. The EWs derived from the color excess are included in Table 2.

### 3.2. EELGs with Extremely High EW

In the J sample, the magnitudes in  $Y_{105}$ ,  $YJ_{110}$  and  $JH_{140}$  are all boosted by  $[\text{O III}]$   $\lambda\lambda 4959, 5007$ , and the derived EWs can be averaged with the errors as weights to make a better constraint. There are two EELGs (J2 and J29) among the 40 EELGs showing EWs above 3000 Å, which are  $3737 \pm 726 \text{ Å}$  and  $3332 \pm 439 \text{ Å}$ . As seen in Figure 7, both of these two EELGs are extremely compact. The FWHM of the instrument point-spread function (PSF) is  $0''.14$  for the  $J_{125}$ , hence the EELGs are all resolved. After subtracting the instrument PSF and the lensing effect, the measured sizes correspond to physical sizes of about 1.7 kpc and 0.9 kpc.

In addition, the EW of Y9 in the Y sample is also measured to be  $3307 \pm 1293 \text{ Å}$ . As only the  $Y_{105}$  is free from contaminations by other emission lines in the Y sample, the EW can be only derived from the excess of the  $Y_{105}$  band and thus contains higher uncertainty. Y9 is also selected as a LBG in Bradley et al. (2013) (B13 hereafter) and we will discuss this candidates in the next section.

The same selection method as our J sample is also utilized for CANDELS field in VDW11. VDW11 identified 69 candidates in a total area of 279 square arcminutes. The typical area coverage over each cluster field in CLASH is  $\sim 4 \text{ arcmin}^2$  indicated from the area available within the WFC3/IR field of view. To count for the influence of the bright galaxies in the fields, we count the areas covered by galaxies based on the segmentation images and subtracted these areas from the total areas indicated from exposure time images. Then the total areas to search EELGs in CLASH fields is  $\sim 112 \text{ arcmin}^2$ . The VDW11 used the data from the Ultra Deep Survey (UDS) field in the wide program, and the GOODS-South Deep (GSD) field at 4-epoch depth in the deep program. The VDW11 sample include 40 and 29 EELGs from these two fields, named as the UDS sample and GSD sample hereafter. The number density for the J sample is 0.36 per square arcminutes, compared to 0.19 per square arcminutes in the UDS sample and 0.39 per square arcminutes in the GSD sample. The high detection rates in the

J sample and the GSD sample are due to the deeper observations. As shown in Figure 8, the J sample is the deepest and can reach about 28.5 mag after correcting the lensing effect. The lensing effect increases the depth and reduces the volume of observations in the meantime, in addition of the small samples, we do not find significant different detection rate between the CLASH fields and the GSD field.

It is apparent in Figure 8 that the EELGs with higher EWs are more common in fainter EELGs. The three EELGs with extremely high EWs are fainter than most candidates. In the VDW sample, only two candidates has EWs larger than 2000 Å, which are  $2304 \pm 515 \text{ Å}$  and  $2002 \pm 849 \text{ Å}$ <sup>23</sup>. Both of these two candidates are selected from the GSD field which are deeper than the UDS field. All these samples support the idea that we can detect EELGs with stronger emission lines in deeper observations. The three extreme candidates are unlikely due to noise fluctuations. We examine the probability that one EELG with  $\text{EW}([\text{OIII}]+H_{\beta} \lambda 4861) = 2000 \text{ Å}$  at the same redshift are measured to be  $\text{EW} \geq 3000 \text{ Å}$ . In our spectral model, fluctuations with the level of 1/3 continua, which are the worst cases in our samples, are added to each band. We simulate the photometry for 10000 times and measure the EWs with the same method. The possibility of spurious large EW ( $\geq 3000 \text{ Å}$ ) is lower than 20%. The rate will reduce to lower than 4%, if the EW are measured with flux excesses in two bands, and the rate will be negligible if there are three bands to constrain the EW. As the spectra in Figure 7 and the results in Table 1, the large EWs are confirmed with three bands for J2 candidate and two bands for J29 candidate. Both the two EELG candidates show similar spectral shapes, moreover, the significant boosts in  $Z_{850}$  and  $Y_{105}$  due to  $[\text{O II}]$   $\lambda 3727$  line are also in agreement with the strong  $[\text{O III}]$  5007 Å line. The EW of Y9 candidate can only be estimate with the boost of  $Y_{105}$ , therefore, the noise fluctuation cannot be totally excluded and the strength could be confirmed with further observations.

VDW11 found these candidates are low-mass ( $\sim 10^8 M_{\odot}$ ) galaxies, starbursting ( $\sim 5 M_{\odot} \text{ yr}^{-1}$ ), young ( $5 \sim 40 \text{ Myr}$ ) galaxies. The nature is also consistent with the spectral observations of two highly lensed EELGs at  $z=1.85$  and  $3.12$  (Brammer et al. 2012; van der Wel et al. 2013, respectively). We estimate the age and stellar mass following the same method as VDW11. In general, we use the Starburst99 model (SB99, Leitherer et al. 1999) with continuous star formation and a Chabrier (2003) IMF with a high-mass cut off at  $100 M_{\odot}$  and metallicity  $0.2 Z_{\odot}$ . The  $\text{EW}(H_{\beta})$  declines as time and is used as an age indicator.  $\text{EW}(H_{\beta})$  is assumed to contribute 1/8 to the combined EW. The upper limit of  $\text{EW}([\text{OIII}]+H_{\beta})$  is 4336 Å from this model and will decrease to 3838 Å if we use a solar metallicity. VDW11 estimated stellar masses based on the rest frame V band luminosity from the  $H_{160}$  band photometry. To increase the accuracy, we use the weighted average photometry of the continue bands instead. The inferred masses are shown in Table

<sup>23</sup> VDW11 used the  $\text{EW}([\text{O III}] \lambda 5007)$  instead of  $\text{EW}([\text{OIII}]+H_{\beta})$  in their table. The  $\text{EW}([\text{O III}] \lambda 5007)$  were calculated by assuming a fixed flux ratio of  $H_{\beta}$  and  $[\text{O III}] \lambda\lambda 4959, 5007$ . Therefore, we obtain the  $\text{EW}([\text{OIII}]+H_{\beta})$  using the same ratios.

1 and Table 2. The median value of  $7.1 \times 10^6 M_\odot$  is one order lower than the VDW sample. Maseda et al. (2013) find similar dynamic mass and the young stellar mass ratios of the VDW sample to other star forming galaxies in  $z \sim 2$ , and confirmed that the low stellar mass are dominated by the intense starbursts. These EELGs provide insight into the evolution of the dwarf galaxies and provide evidence that the starburst phase plays a key role in the mass build-up for at least some low mass galaxies.

#### 4. DISCUSSION

Strong emission lines are known to have a significant impact on the SED fitting (Atek et al. 2011; Schaerer & de Barros 2009; Labbé et al. 2010, 2012; Stark et al. 2013; Shim et al. 2011; Fumagalli et al. 2012). Labbé et al. (2012) investigated the ultra-deep Spitzer/IRAC photometry for a sample of  $z \sim 8$  galaxies from the Hubble UDF program and found an average contribution of  $\sim 0.44$  mag to the [4.5] band of Spitzer by [O III]  $\lambda\lambda 4959, 5007$ . Schaerer & de Barros (2009) found that the apparent Balmer breaks observed in a number of  $z \sim 6$  galaxies detected at  $> 3.6 \mu\text{m}$  with Spitzer/IRAC can be explained by the presence of redshifted strong emission lines. Smit et al. (2014) select galaxies at narrow redshift range  $z \sim 6.6\text{--}7.0$  to avoid contamination of other emission lines and detected very high [OIII] +  $H_\beta$  lines. The mean value of  $EW([OIII] + H_\beta)$  derived from the excesses of  $3.6 \mu\text{m}$  band is greater than  $637 \text{ \AA}$  with one extreme EW of  $1582 \text{ \AA}$ . Shim et al. (2011) also found that the fraction of emission line galaxies evolves with redshift and that emission-line galaxies could be more common in high redshifts. However, properly considering the impact is still a challenge due to the lack knowledge of such galaxies. The EELG samples are the median redshift analogs and provide a good opportunity to study the high redshift star forming galaxies.

While emission lines have been considered in galaxy templates (Schaerer & de Barros 2009; Ono et al. 2010), the high redshift galaxy selection itself can also be affected due to the exist of median redshift EELGs. The fainter and stronger EELGs in our samples indicate that the impact of EELGs to the selection of LBG has probably been underestimated. The properties of LBG could be misunderstood due to the mix of these EELGs. Taniguchi et al. (2010) investigated the EELG interlopers for  $z \sim 8$  galaxies in the Hubble Ultra Deep Field. The EWs of [O III]  $\lambda 5007$  in their models only vary up to  $\sim 1000 \text{ \AA}$ , therefore they claimed a negligible probability for low-redshift interlopers. Considering the EELGs with  $EW([OIII] + H_\beta) \geq 3000 \text{ \AA}$  in our sample and the strong [O III]  $\lambda 5007$  and  $H\alpha \lambda 6563$  in other surveys (Cardamone et al. 2009; Atek et al. 2011; Brammer et al. 2012; Shim & Chary 2013; van der Wel et al. 2013; Smit et al. 2014), it is necessary to reexamine the impact of EELGs on the selections of LBG.

##### 4.1. Contamination to the Selection of $z \sim 6$ Galaxies

Firstly, we test whether any sources in our samples would satisfy the color selections for LBG. From Figure 1, both the terms of  $J_{125} - I_{814}$  in the J sample and  $Y_{105} - I_{814}$  in the Y sample can reach more than one magnitude. In the color-color selections of LBG, a decrement of one magnitude is adopted (Bouwens et al. 2012;

Zheng et al. 2012; Oesch et al. 2012, 2013). Furthermore, a candidate at  $z > 7$  must not be detected in the optical bands. For the bright EELGs in our samples, their continuum from near infrared to UV bands is detected with high confidence. However, there are still a few EELGs with faint continua and the bands bluer than  $I_{814}$  fall below the detection limit, resulting in mimic LBG with redshift around 6. When the S/N ratio is low, it becomes difficult to distinguish whether the color excess is due to the Lyman break as seen in LBG or the boost by strong emission lines in EELGs.

Recently, B13 reported a considerable number of galaxy candidates at  $z \sim 6 - 8$  in 18 CLASH clusters (Abell 1423, Abell 209, CLJ1226.9+3332, MACS0429.6-0253, MACS1311.0-0310, MACS1423.8+2404, RXJ2129.7+0005 are not included compared to the total of 25 clusters). Their selections are based on the redshifts calculated from Bayesian photometric redshift (BPZ) code (Benítez 2000). This method also identifies high redshift galaxy candidates primarily based on the Lyman break feature and the results are generally in very good agreement with the common color-color selection method. Possible contaminations of EELGs at the high redshift samples are shown by matching the samples to our EELGs. Two EELGs, Y8 and Y9, are also selected as m1115-0352 ( $z=6.2$ ) and m1720-1114 ( $z=5.9$ ) in the  $z \sim 6$  sample of B13. Another galaxy in Abell 209 (RA: 22.954264, DEC: -13.611176), which is removed out from the Y sample because the  $I_{814}$  band detection is below  $3\sigma$ , is also included for its high photometric redshift (5.89) from BPZ and is called Y0. These candidates have similar spectra shapes as shown with solid black circles in Figure 9. The best BPZ results are shown with open orange boxes. We also fit the  $I_{814}$  band and redward bands with our strong emission line model which is shown with blue boxes. In the emission line model, we fix the spectral slope to 2 and the  $EW([OIII] + H_\beta)$  to be the value estimated with  $Y_{105}$  band excess. Emission lines with flux ratios from a  $0.2Z_\odot$  galaxy (Anders & Fritze-v. Alvensleben 2003) are considered. The only two free parameters left are the redshift and the normalization. While the high redshift assumption often fails to fit the  $H_{160}$  band, our emission line model can explain the drop of flux in  $H_{160}$  bands in three galaxies. The emission line model also overestimate the flux in the  $Y_{814}$  band. The  $\chi^2$  values are shown with the same colors in the figure. For all the three candidates, the spectra favor the emission line models for the slightly lower  $\chi^2$  values.

If such candidates are chosen as LBG, the UV-continuum slopes derived from infrared bands would be misleading. We estimate the slopes for the three candidates with a linear fitting method for the bands redder than the  $I_{814}$  band. The derived UV slopes are  $3.7 \pm 0.5$ ,  $3.6 \pm 0.5$  and  $3.5 \pm 0.4$  for Y0, Y8 and Y9, respectively. Bouwens et al. (2010) obtain the UV-continuum slopes for redshift 6 galaxies with  $Y_{105}$ ,  $J_{125}$  and  $H_{160}$ . Using the same method, we get even bluer slopes which are  $4.5 \pm 0.8$ ,  $4.9 \pm 0.9$  and  $4.4 \pm 0.6$ . These values are all at least  $1\sigma$  bluer than the mean UV-continuum slope in redshift 6 (Bouwens et al. 2010). Nevertheless, the current CLASH data and Spitzer/IRAC data are not deep enough to confirm the nature of these galaxies. Our EELG color-color selections are limited by the luminos-

ity of continuum. Much more EELGs with stronger emission lines are faint and below our detection limit according to the EW and luminosity trend. What is more, our samples only include EELGs in specific redshift ranges. Therefore, the total contamination of EELGs to the high redshift sample of B13 can be higher.

#### 4.2. Impact on the Selection of $z \sim 10$ Galaxies

Recently, the search for LBG has reached  $z \sim 10$  (Zheng et al. 2012; Bouwens et al. 2013a; Ellis et al. 2013; Coe et al. 2013; Oesch et al. 2013). One of them, UDFj-39546284, has already been found to be possibly an EELG at redshift  $\sim 2$  (Brammer et al. 2013; Capak et al. 2013). More candidates are found in the ongoing Hubble Frontier Fields (Zheng et al. 2014; Zitrin et al. 2014; Ishigaki et al. 2014). As there is no enough spectral observations to confirm the redshifts, properly considering the contamination of EELGs are quite necessary for these samples.

For galaxies with  $z \sim 8.7 - 10.5$ , the  $\text{Ly}\alpha$ -break shifts into the  $JH_{140}$  band and could be selected as  $J_{125}$  drop-out. If the redshift is higher than 10.5, the  $\text{Ly}\alpha$ -break has shifted out of the  $J_{125}$  band, and only  $H_{160}$  and parts of  $JH_{140}$  cover the continuum. EELGs with strong emission lines falling in the  $H_{160}$  band can also mimic such spectral feature. Considering a power-law spectrum with  $\text{EW}([\text{OIII}]+H_{\beta}) = 2000(3000) \text{ \AA}$  in our model, the dropout  $J_{125} - H_{160} \sim 1.1(1.4)$  would be observed for EELGs at redshift 1.9. Taking into account the deviation of the slopes which would increase the observed color difference in EELGs, we propose that, unlike current HST WFC3/IR surveys in CLASH or UDF12, at least one mag deeper observations in the bluer bands will be required to constrain the flux of the continuum and draw a distinction between these two scenarios. In EELGs at the matched redshift, the  $\text{H}\alpha$   $\lambda 6563$  has moved out of the  $H_{160}$  band, but the impact of  $[\text{O II}] \lambda 3727$  on  $J_{125}$  cannot be neglected, therefore the deeper observations in the  $Y_{105}$  or  $YJ_{110}$  bands will be helpful. If a deeper observation is not available, a significant detection in Spitzer observation are required to confirm the high redshift LBG (Zheng et al. 2012; Oesch et al. 2013). Real high redshift LBG have a flat UV continuum and the detection from  $H_{160}$  band to mid-infrared bands cannot be mimicked by any type of EELGs.

#### 4.3. EELG Fraction in High Redshift Samples

While it is almost impossible to distinguish EELGs and high redshift galaxies without spectroscopic observations, we should consider that there is a certain number of EELGs in the high redshift galaxies. The spectral features of our J and Y samples are similar to the  $I_{814}$  and  $Y_{105}$  dropout galaxies at redshift range 5.6-8.0. The B13 sample includes a total of 206 galaxies in this redshift range and we find two galaxies common as our EELG samples. If the both of these two galaxies are EELGs, the contamination fraction for the B13 sample is at least  $2/206 \sim 1\%$ . However, the real contamination fraction could be higher due to the limit of observations. Our EELG samples only include such candidates that the continua are detected higher than  $3\sigma$  in  $I_{814}$ . There are substantial fainter EELGs which probably include stronger emission lines (See the trend in Figure 8).

Recently, the frontier of high redshift samples are redshift higher than 9 selected based on the  $J_{125}$  drop-out. The fraction of EELGs in these  $J_{125}$  drop-out samples will be more significant than the contamination in B13 sample. Firstly, these  $J_{125}$  drop-out samples are in redshift range 8.7-10.5 and can be contaminated by EELGs in redshift range 1.8-2.2. The comoving volume of the redshift range 1.8-2.2 is 1.1 times of the total volume of the Y and J samples. Meanwhile, the comoving volume of the  $J_{125}$  drop-out samples is 0.6 times of the  $I_{814}$  drop-out samples. In the same projected area, there will be  $1.1/0.6 \sim 1.8$  times more contaminations due to EELGs. Secondly, the buildup of star-forming galaxies peak at near redshift 2 which means there are a substantial population of EELGs in that redshift. From the median redshift of our EELG samples 1.5 to redshift 1.9, the space density of star forming galaxies increases by 2.3 times (Oesch et al. 2010). Moreover, the space densities of star-forming galaxies decline since redshift around 2 (Bouwens et al. 2014). From redshift 6 to redshift 9, the space density of galaxies decreases about ten times. All of these will result in that there are the EELG contamination fraction for the  $J_{125}$  drop-out samples will be  $1.8 \times 2.3 \times 10 \approx 41$  times higher. Pirzkal et al. (2013) develops a Markov Chain Monte Carlo (MCMC) fitting method with the ability to accurately estimate the probability density function of the redshift for each object. After the analysis of the redshift 8-12 galaxy sample, they report that there is an average probability of 21% that these well defined high redshift galaxies are low redshift interlopers.

Without infrared or deeper HST observations, these EELG contamination can not be completely excluded. Therefore, it is quite necessary to properly include the contamination fraction of EELGs for the analysis of high redshift samples. However, the contamination fraction is still large uncertain due to the lack of observations of EELGs. The ongoing Hubble Frontier Fields program devote a total 560 orbits to observe four clusters along with four parallel blank fields. This initiative can reach 5 $\sigma$  magnitude limit of  $\sim 28.7$  which is 1.2 deeper than CLASH field. A systematical selections of EELGs in the Hubble Frontier Fields will help us to constrain the number density of faint EELGs and resolve the EELG contamination fraction for high redshift galaxies.

#### 5. SUMMARY

We have carried out two color-color selections to search for EELGs with  $\text{EW} > 600 \text{ \AA}$  in 25 CLASH cluster fields. We identified two samples consisting of 40 and 12 EELGs, in redshift ranges  $1.55 \sim 1.79$  and  $0.93 \sim 1.14$ , respectively. Thanks to cluster lensing, EELGs are detected down to intrinsic apparent magnitude 28.5, which is significantly fainter than other samples. Three candidates are found with extreme  $\text{EW} > 3000 \text{ \AA}$ , which are stronger than other surveys. We found an abundant population of low-luminosity galaxies whose emission lines are considerably stronger than other samples. These EELGs are considered as low mass and strong starburst galaxies in the early stage. Future deep spectral observations are needed for such low luminosity galaxies.

Strong emission lines in these EELGs can boost the broadband photometry by more than one magnitude. Such extreme emission lines will not only impact the SED



fitting, but also mimic the dropout feature seen in LBG and contaminate the selections. We compare the EELGs and the LBG selected from the CLASH data (Bradley et al. 2013), and find two common objects in our Y sample and the  $z \sim 6$  galaxies. Both the EELGs and the LBGs can explain the spectral type, but the current photometric data are not deep enough to definitely distinguish between the two scenarios. We also notice that the possible contamination for future selections of galaxies at  $z \sim 10$  cannot be ignored and the contamination fraction could be significantly higher. One magnitude deeper observations in the bluer bands ( $Y_{105}$  or  $Y_{J110}$ ) or the detection in mid-infrared bands with Spitzer/IRAC may help us identify the real LBG.

Future deep spectroscopic observations of EELGs like James Webb Space Telescope (JWST) are needed to make accurate measurements of emission lines and unveil the nature of these EELGs. Furthermore, the ongoing *HST* observations of frontier fields provides unprecedented deep observations of six clusters and six parallel fields<sup>24</sup>. We predict that these deep observations will reveal dozens of EELGs with possible stronger emission lines, which will help us to confirm the EW and luminosity trend and estimate the number density.

*Facilities:* HST (ACS,WFC3)

The CLASH program (GO-12065) is based on observations made with the NASA/ESA *Hubble Space Telescope*. The Space Telescope Science Institute is operated by the Association of Universities for Research in Astronomy, Inc. under NASA contract NAS 5-26555. J.X.W. acknowledges support from Chinese Top-notch Young Talents Program and the Strategic Priority Research Program “The Emergence of Cosmological Structures” of the Chinese Academy of Sciences (grant No. XDB09000000).

## REFERENCES

- Anders, P., & Fritze-v. Alvensleben, U. 2003, *A&A*, 401, 1063
- Atek, H., Siana, B., Scarlata, C., \*, et al. 2011, *ApJ*, 743, 121
- Atek, H., Kneib, J.-P., Pacifici, C., et al. 2014, *ApJ*, 789, 96
- Bennert, N., Jungwiert, B., Komossa, S., Haas, M., & Chini, R. 2006, *A&A*, 459, 55
- Benítez, N. 2000, *ApJ*, 536, 571
- Bertin, E., & Arnouts, S. 1996, *A&AS*, 117, 393
- Blakeslee, J. P., Anderson, K. R., Meurer, G. R., Benítez, N., & Magee, D. 2003, *Astronomical Data Analysis Software and Systems XII*, 295, 257
- Bouwens, R. J., Illingworth, G. D., Franx, M., et al. 2009, *ApJ*, 705, 936
- Bouwens, R. J., Illingworth, G. D., Oesch, P. A., et al. 2010, *ApJ*, 708, L69
- Bouwens, R. J., Illingworth, G. D., Labbé, I., et al. 2011, *Nature*, 469, 504
- Bouwens, R., Bradley, L., Zitrin, A., et al. 2012, [arXiv:1211.2230](#)
- Bouwens, R. J., Illingworth, G. D., Oesch, P. A., et al. 2012, *ApJ*, 754, 83
- Bouwens, R. J., Oesch, P. A., Illingworth, G. D., et al. 2013a, *ApJ*, 765, L16
- Bouwens, R. J., Illingworth, G. D., Oesch, P. A., et al. 2014, [arXiv:1403.4295](#)
- Bradley, L. D., Zitrin, A., Coe, D., et al. 2013, [arXiv:1308.1692](#)
- Brammer, G. B., Sánchez-Janssen, R., Labbé, I., et al. 2012, *ApJ*, 758, L17
- Brammer, G. B., van Dokkum, P. G., Illingworth, G. D., et al. 2013, [arXiv:1301.0317](#)
- Chabrier, G. 2003, *PASP*, 115, 763
- Calzetti, D. 2008, *Pathways Through an Eclectic Universe*, 390, 121
- Capak, P., Faisst, A., Vieira, J. D., et al. 2013, *ApJ*, 773, L14
- Cardamone, C., et al. 2009, *MNRAS*, 399, 1191
- Cardelli, J. A., Clayton, G. C., & Mathis, J. S. 1989, *ApJ*, 345, 245
- Coe, D., Zitrin, A., Carrasco, M., et al. 2013, *ApJ*, 762, 32
- Ellis, R. S., McLure, R. J., Dunlop, J. S., et al. 2013, *ApJ*, 763, L7
- Erb, D. K., Steidel, C. C., Shapley, A. E., et al. 2006, *ApJ*, 647, 128
- Finkelstein, S. L., Papovich, C., Dickinson, M., et al. 2013, [arXiv:1310.6031](#)
- Frye, B. L., Hurley, M., Bowen, D. V., et al. 2012, *ApJ*, 754, 17
- Fumagalli, M., Patel, S. G., Franx, M., et al. 2012, *ApJ*, 757, L22
- Gonzaga, S., Hack, W., Fruchter, A., Mack, J., eds. 2012, *The DrizzlePac Handbook*. (Baltimore, STScI)
- Grogin, N. A., Kocevski, D. D., Faber, S. M., et al. 2011, *ApJS*, 197, 35
- Hu, E. M., Cowie, L. L., Kakazu, Y., & Barger, A. J. 2009, *ApJ*, 698, 2014
- Ishigaki, M., Kawamata, R., Ouchi, M., et al. 2014, [arXiv:1408.6903](#)
- Kakazu, Y., Cowie, L. L., & Hu, E. M. 2007, *ApJ*, 668, 853
- Kauffmann, G., Heckman, T. M., Tremonti, C., et al. 2003, *MNRAS*, 346, 1055
- Kewley, L. J., Geller, M. J., & Jansen, R. A. 2004, *AJ*, 127, 2002
- Koekemoer, A. M., Fruchter, A. S., Hook, R. N., & Hack, W. 2003, *HST Calibration Workshop : Hubble after the Installation of the ACS and the NICMOS Cooling System*, 337
- Koekemoer, A. M., Faber, S. M., Ferguson, H. C., et al. 2011, *ApJS*, 197, 36
- Labbé, I., et al. 2010, *ApJ*, 716, L103
- Labbé, I., Oesch, P. A., Bouwens, R. J., et al. 2012, [arXiv:1209.3037](#)
- Lequeux, J., Peimbert, M., Rayo, J. F., Serrano, A., & Torres-Peimbert, S. 1979, *A&A*, 80, 155
- Leitherer, C., Schaerer, D., Goldader, J. D., et al. 1999, *ApJS*, 123, 3
- Mannucci, F., Salvaterra, R., & Campisi, M. A. 2011, *MNRAS*, 414, 1263
- Maseda, M. V., van der Wel, A., da Cunha, E., et al. 2013, *ApJ*, 778, L22
- Oesch, P. A., Bouwens, R. J., Carollo, C. M., et al. 2010, *ApJ*, 725, L150
- Oesch, P. A., Bouwens, R. J., Illingworth, G. D., et al. 2012, *ApJ*, 759, 135
- Oesch, P. A., Bouwens, R. J., Illingworth, G. D., et al. 2013, [arXiv:1309.2280](#)
- Ono, Y., Ouchi, M., Shimasaku, K., et al. 2010, *MNRAS*, 402, 1580
- Pirzkal, N., Rothberg, B., Ryan, R., et al. 2013, *ApJ*, 775, 11
- Postman, M., Coe, D., Benítez, N., et al. 2012, *ApJS*, 199, 25
- Rajan, A. et al. 2010, “WFC3 Data Handbook”, Version 2.1, (Baltimore: STScI).
- Reddy, N. A., Steidel, C. C., Pettini, M., et al. 2008, *ApJS*, 175, 48
- Reddy, N. A., & Steidel, C. C. 2009, *ApJ*, 692, 778
- Salzer, J. J., Lee, J. C., Melbourne, J., et al. 2005, *ApJ*, 624, 661
- Schaerer, D., & de Barros, S. 2009, *A&A*, 502, 423
- Shim, H. & Chary, R. 2013, *ApJ*, 765, 26
- Shim, H., Chary, R., Dickinson, M., Lin, L., Spinrad, H., Stern, D., Yan, C. 2011, *ApJ*, 738, 69
- Smit, R., Bouwens, R. J., Labbé, I., et al. 2014, *ApJ*, 784, 58
- Stark, D. P., Schenker, M. A., Ellis, R., et al. 2013, *ApJ*, 763, 129
- Straughn, A. N., et al. 2009, *AJ*, 138, 1022
- Storey, P. J., & Hummer, D. G. 1995, *MNRAS*, 272, 41
- Taniguchi, Y., Shioya, Y., & Trump, J. R. 2010, *ApJ*, 724, 1480
- Trump, J. R., Weiner, B. J., Scarlata, C., et al. 2011, [arXiv:1108.6075](#)
- van der Wel, A., Straughn, A. N., Rix, H.-W., et al. 2011, *ApJ*, 742, L11
- van der Wel, A., van de Ven, G., Maseda, M., et al. 2013, [arXiv:1309.2826](#)

<sup>24</sup> For details, see <http://www.stsci.edu/hst/campaigns/frontier-fields/>

- Vanden Berk, D. E., Richards, G. T., Bauer, A., et al. 2001, AJ, 122, 549
- Zitrin, A., Broadhurst, T., Umetsu, K., et al. 2009, MNRAS, 396, 1985
- Zitrin, A., Broadhurst, T., Coe, D., et al. 2011, ApJ, 742, 117
- Zitrin, A., Zheng, W., Broadhurst, T., et al. 2014, ApJ, 793, L12
- Zheng, W., Bradley, L. D. Saraff, A. et al. 2012a, in Seventh Conference on Astronomical Data Analysis, <http://ada7.cosmostat.org/proceedings.php>, 17
- Zheng, W., Postman, M., Zitrin, A., et al. 2012, Nature, 489, 406
- Zheng, W., Shu, X., Moustakas, J., et al. 2014, [arXiv:1402.6743](https://arxiv.org/abs/1402.6743)



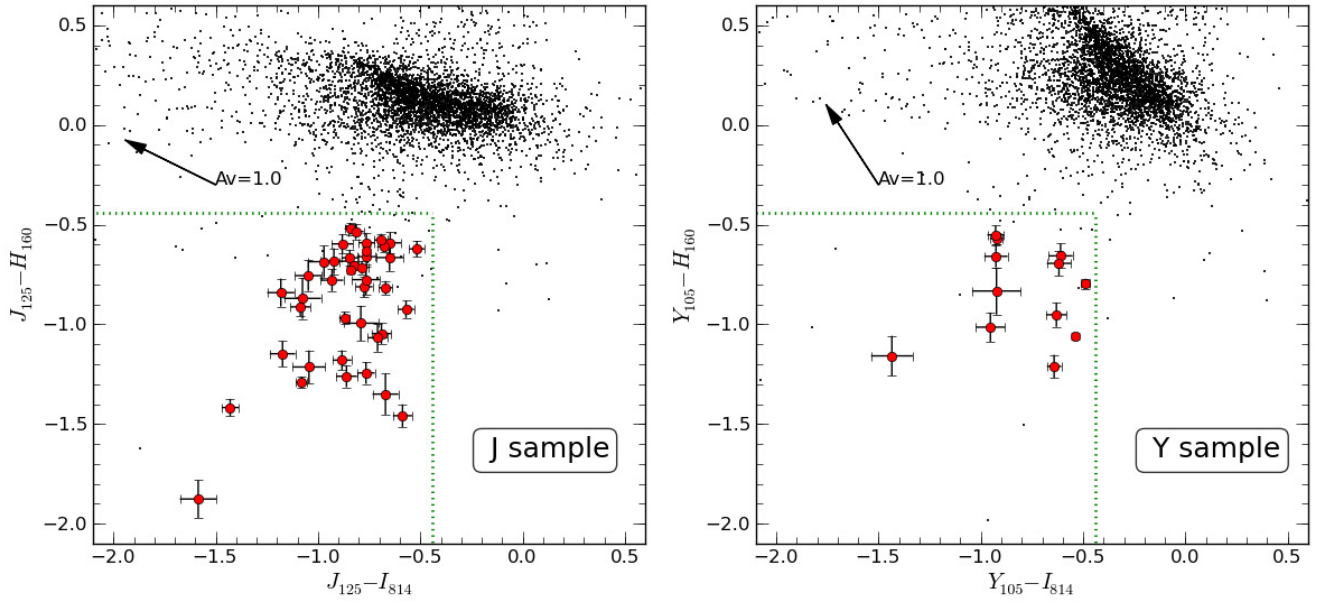


**Figure 1.** Color-color diagrams to select the EELG candidates. The red circles with error bars mark the selected EELGs and the black points mark all objects in the CLASH fields. The regions separated by dash lines represent our selection criteria. The black arrows illustrate the effect of dust attenuation using the formula from [Cardelli et al. \(1989\)](#).

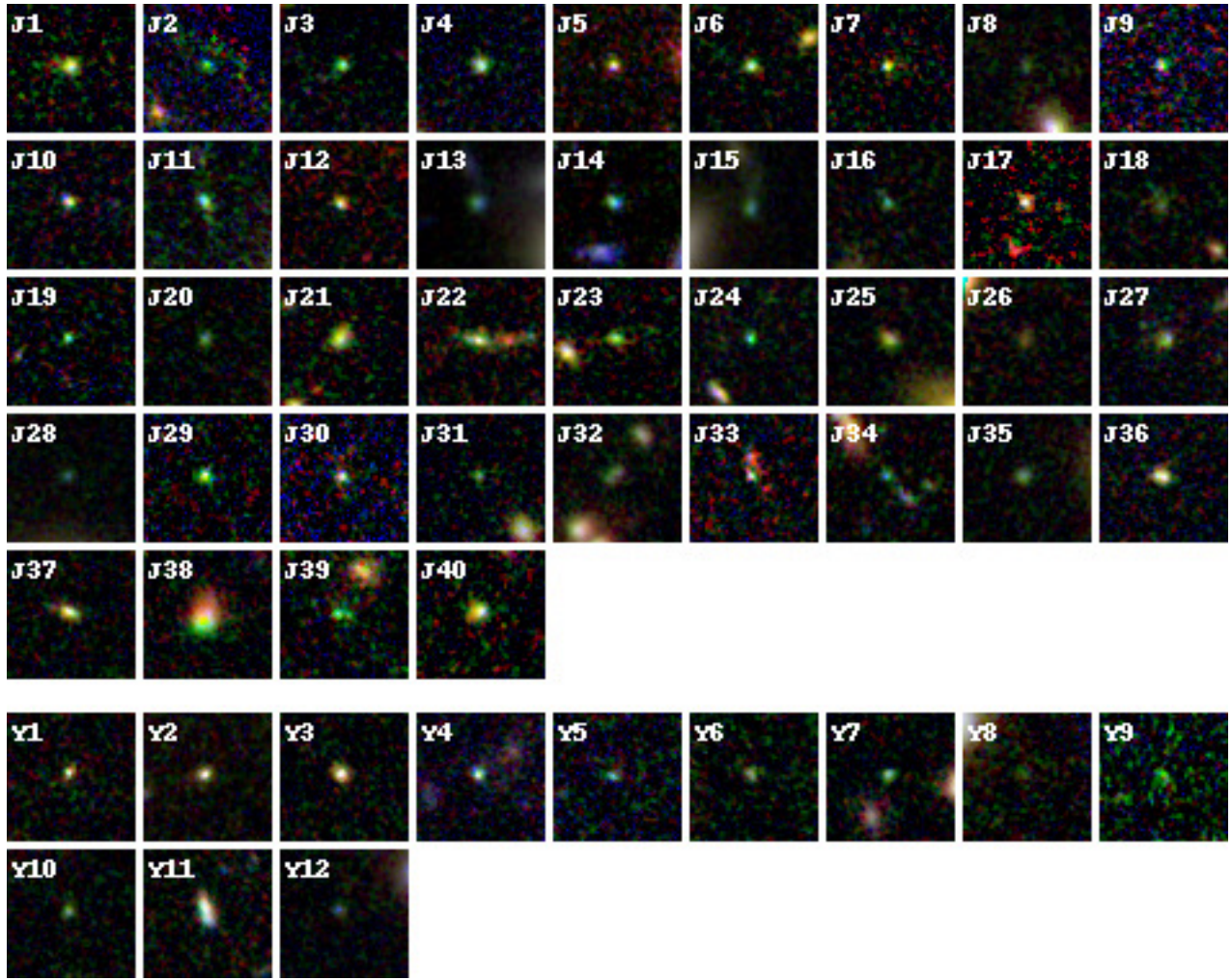


**Figure 2.** Composite color images for the J and Y samples created with the same three bands as used for the selections. The center peak bands are presented with green color, while the continuum bands are presented with blue and red colors. The width of each stamp image is 50 pixels and the pixel size is  $0.065''/\text{pixel}$ .

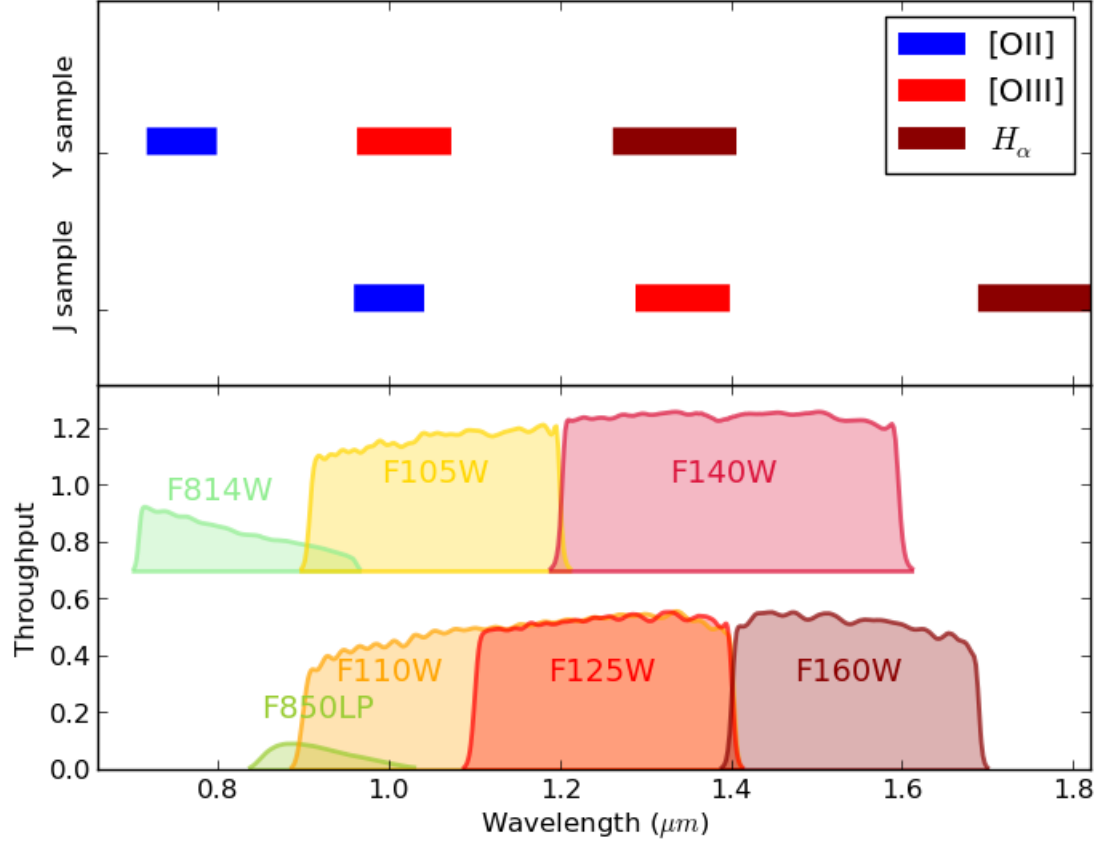


**Figure 3.** Wavelength ranges of strong emission lines in our J and Y samples. The top panel shows the wavelength ranges for [OII], [OIII] and  $H_\alpha$  with the redshifts of the J sample and the Y sample. The lower panel shows the throughputs of the *HST* filters. There is a total of 16 filters used in the CLASH observations, but only the redward filters related to strong emission lines is shown here,

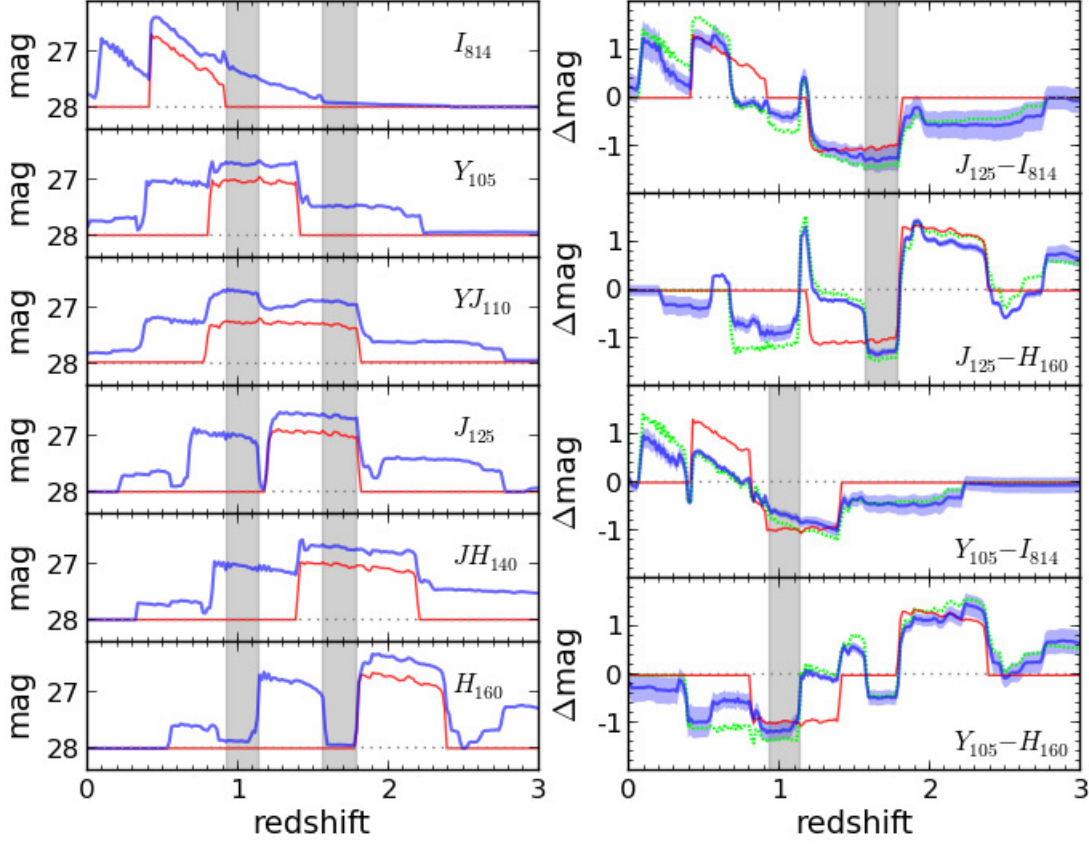


**Figure 4.** Effect of strong emission lines on the photometry as a function of redshift estimated with our spectral model. The spectral model represents the spectrum of a star-forming galaxy, which consists of a power-law spectrum and strong emission lines with the flux ratios from [Anders & Fritze-v. Alvensleben \(2003\)](#). In the left panels, photometry of six bands used in the EW calculations are plotted versus the redshift. In the right panels, the colors used for our selections are plotted versus redshift (upper: the J sample, lower: the Y sample). In the spectral model, the two set of emission line ratios for metallicity  $Z = 0.2Z_{\odot}$  and  $Z = 0.02Z_{\odot}$  are considered, which are shown with blue lines and green dotted lines. The blue shadows around the blue lines in the right panels present the influence of spectral slope which changes from 1.5 to 2.5. The contributions of [O III]  $\lambda\lambda 4959, 5007$  lines are shown with red lines. Our two color-color selections are quite effective for selections of EELGs in two two redshift ranges ( $0.93 - 1.14$  and  $1.57 - 1.79$ ) marked with gray boxes.

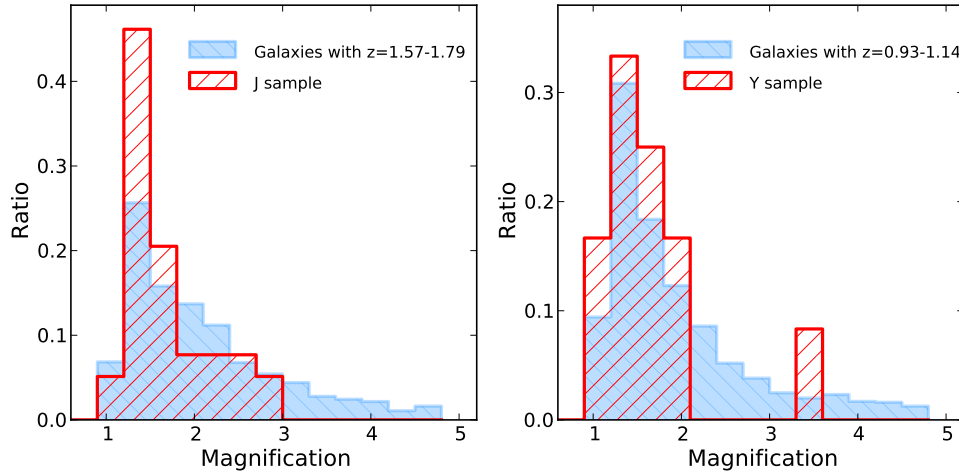


**Figure 5.** Magnification distributions of our J and Y samples (red histograms) and galaxies in the same redshift ranges from the cluster fields (blue filled histograms).



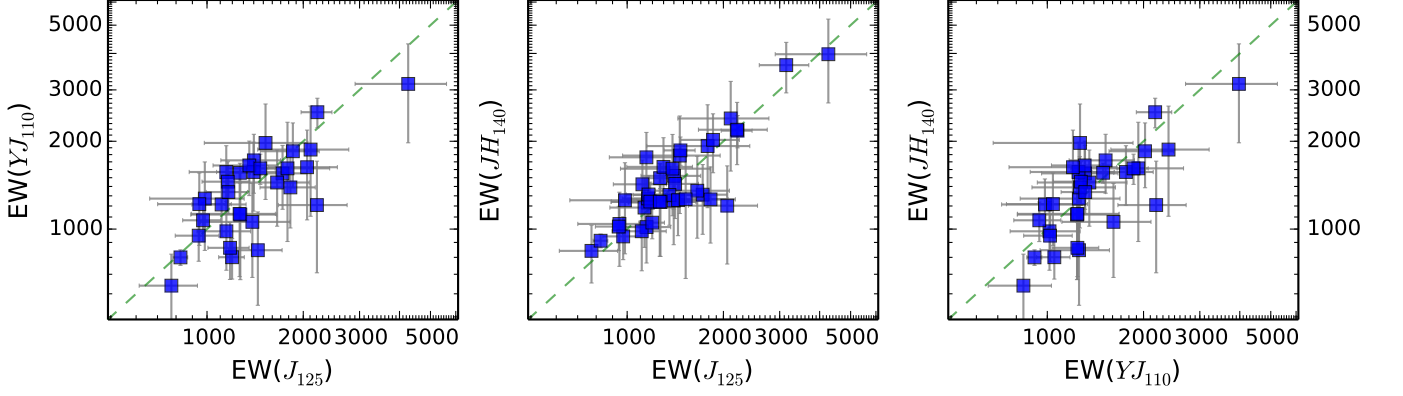


**Figure 6.** Comparison of EWs derived from the color excesses in three different bands for the J sample with the method described in section 3.1. In these calculations, the continua are derived from  $Y_{814}$  and  $H_{160}$ , but the EWs are derived from the excesses of  $YJ_{110}$ ,  $J_{125}$  and  $JH_{140}$ , respectively. The widths of  $YJ_{110}$  and  $JH_{140}$  are broader than  $J_{125}$ , thus the EWs derived from these two bands involve larger uncertainties. The consistency between EWs suggests the robustness of the EW measurements.

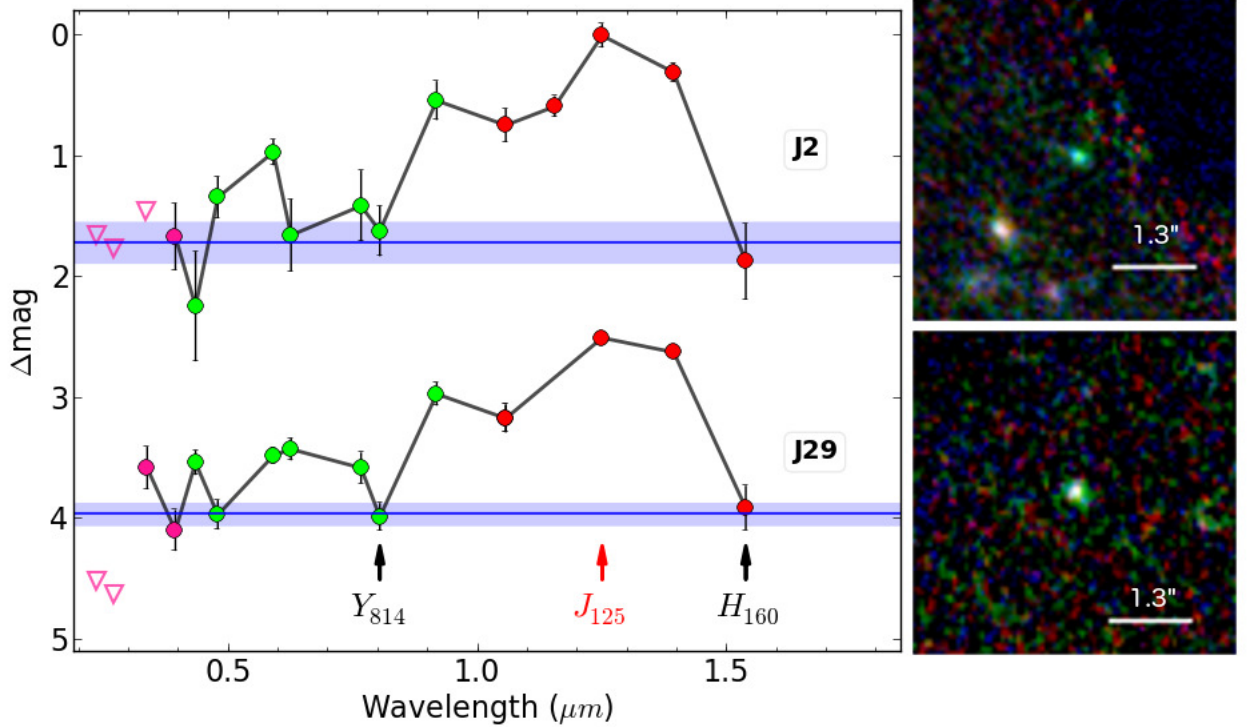


**Figure 7.** SED for the two EELGs with  $EW \sim 3000 \text{ \AA}$  in the J sample (pink: WFC3/UVIS bands, green: ACS, and red: WFC3/IR). The black and red arrows show the central wavelengths of  $I_{814}$ ,  $J_{125}$  and  $H_{160}$  that are used in our selection. The solid blue lines are the estimated continuum levels based on the  $I_{814}$  and  $H_{160}$ , and the shaded regions show the  $1\sigma$  error. The source fluxes are remarkably boosted by strong emission lines up to 1.5 magnitude. The composite color images in the right are created with  $I_{814}$  and  $Y_{105}$  (blue),  $YJ_{110}$ ,  $J_{125}$  and  $JH_{140}$  (green),  $H_{160}$  (red).

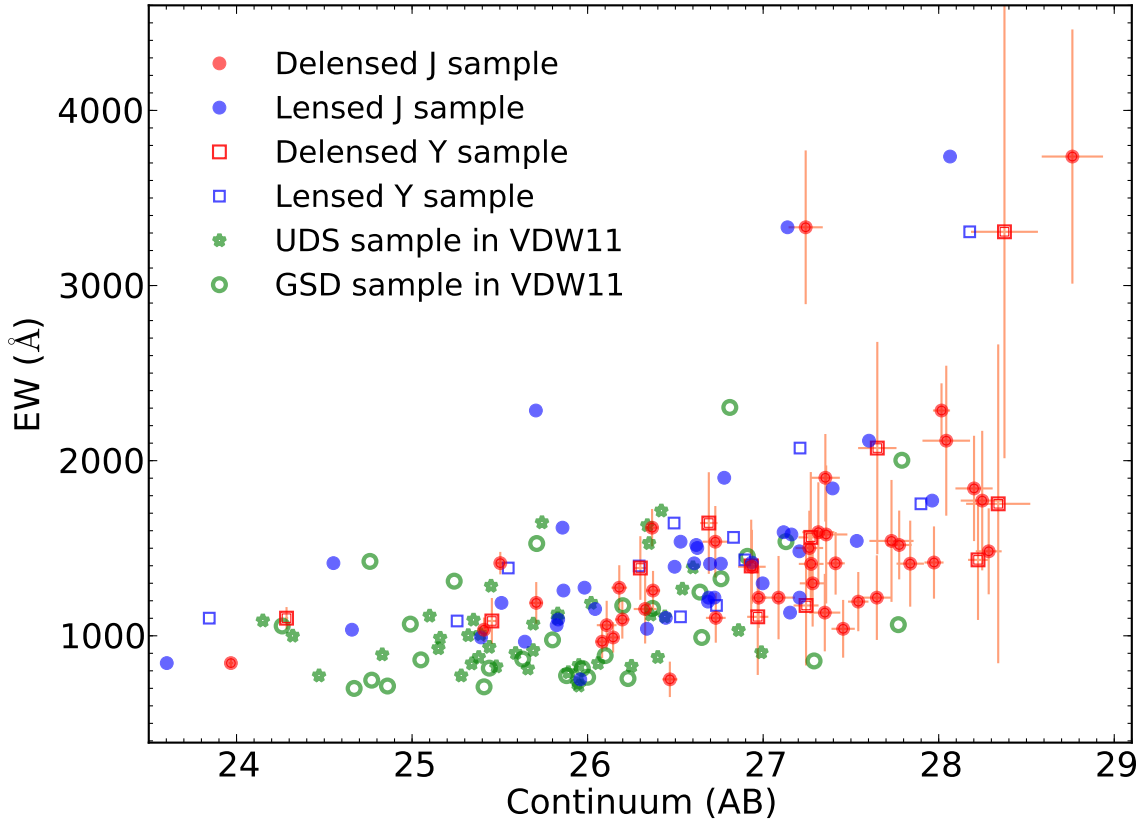


**Figure 8.** EW vs. continuum luminosity for EELGs in the J and Y samples and the UDS and GSD samples from VDW11. The J and Y samples are marked with filled circles and open squares, in which the observed magnitudes are shown in blue color and the intrinsic (delensed) values are shown in red color. As a comparison, the UDS and GSD samples are plotted with green stars and circles. EWs in the J sample are the weighted averages of the three EWs calculated from three different bands. EWs in the Y sample are calculated with the excesses in the  $Y_{105}$  only.

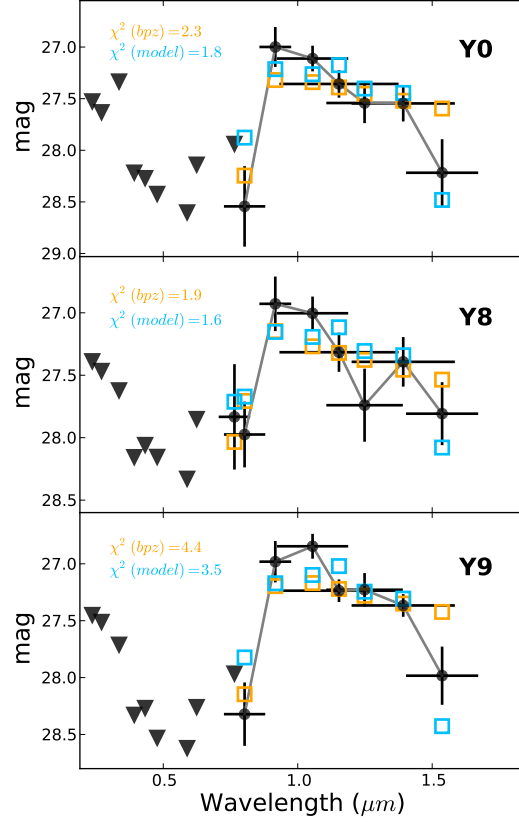


**Figure 9.** Observed magnitudes and best-fit SED of three EELG candidates that can also be selected out as high redshift LBGs. The observed photometries are shown with black circles and the triangles represent the  $2\sigma$  detection limits. All four objects display color excesses near the  $Y_{105}$  which can be fit with both LBG model (orange open squares) and the EELG model (blue open squares). In the EELG model, the spectral slope is fixed to 2 and  $\text{EW}([\text{OIII}]+H_{\beta})$  is fixed to the value estimated from color excesses in  $Y_{105}$ . Other metal emission lines with the flux ratios of stellar metallicity with  $0.2Z_{\odot}$  (Anders & Fritze-v. Alvensleben 2003) have been added. The only two free parameters in the models are the redshift and normalization factor.

**Table 1**  
EELG in the Y Sample

EELG	Cluster	RA	DEC	$I_{814}$	$J_{125}$	$H_{160}$	$EW_{YJ110}$	$EW_{J125}$	$EW_{JH140}$	$\beta$	$\mu$	$FWHM$	$\log(M)$
(1)	(2)	deg (3)	deg (4)	AB (5)	AB (6)	AB (7)	$\text{\AA}$ (8)	$\text{\AA}$ (9)	$\text{\AA}$ (10)	(11)	(12)	arcsec (13)	$M_{\odot}$ (14)
J1	a1423	179.33289	33.60424	25.88 $\pm$ 0.06	25.37 $\pm$ 0.05	25.99 $\pm$ 0.07	640 $\pm$ 181	774 $\pm$ 160	842 $\pm$ 188	1.4 $\pm$ 0.1	1.6	0.37	7.8 $\pm$ 0.2
J2 <sup>a</sup>	a209	22.95528	-13.60011	27.92 $\pm$ 0.21	26.33 $\pm$ 0.10	28.21 $\pm$ 0.32	3145 $\pm$ 1169	4259 $\pm$ 1354	3976 $\pm$ 1270	2.1 $\pm$ 0.4	1.9	0.29	6.7 $\pm$ 6.7
J3	a209	22.98728	-13.60416	26.38 $\pm$ 0.09	25.49 $\pm$ 0.05	26.67 $\pm$ 0.13	1552 $\pm$ 383	1723 $\pm$ 329	1312 $\pm$ 352	2.2 $\pm$ 0.1	1.2	0.25	7.2 $\pm$ 0.1
J4	a209	22.98267	-13.60450	25.91 $\pm$ 0.08	25.07 $\pm$ 0.05	25.73 $\pm$ 0.07	983 $\pm$ 260	1150 $\pm$ 219	1016 $\pm$ 251	1.7 $\pm$ 0.1	1.3	0.28	7.7 $\pm$ 0.2
J5	a383	42.01418	-3.54037	26.80 $\pm$ 0.11	25.92 $\pm$ 0.06	26.51 $\pm$ 0.09	1569 $\pm$ 362	1149 $\pm$ 269	1762 $\pm$ 382	2.0 $\pm$ 0.2	1.7	0.27	6.7 $\pm$ 0.1
J6	a383	42.00668	-3.54478	26.25 $\pm$ 0.07	25.68 $\pm$ 0.05	26.61 $\pm$ 0.10	1215 $\pm$ 271	1111 $\pm$ 214	983 $\pm$ 264	2.4 $\pm$ 0.1	1.2	0.26	7.1 $\pm$ 0.1
J7	a383	42.00755	-3.54529	27.10 $\pm$ 0.12	26.45 $\pm$ 0.08	27.12 $\pm$ 0.13	1272 $\pm$ 427	984 $\pm$ 323	1255 $\pm$ 433	2.2 $\pm$ 0.2	1.2	0.30	6.9 $\pm$ 0.2
J8	c1226	186.75410	33.54530	27.24 $\pm$ 0.09	26.20 $\pm$ 0.10	26.95 $\pm$ 0.13	1444 $\pm$ 421	1657 $\pm$ 432	1353 $\pm$ 423	2.1 $\pm$ 0.2	2.7	0.41	6.7 $\pm$ 0.1
J9	c1226	186.75931	33.53572	27.98 $\pm$ 0.15	26.90 $\pm$ 0.12	27.77 $\pm$ 0.22	1615 $\pm$ 709	1785 $\pm$ 634	1926 $\pm$ 742	3.2 $\pm$ 0.2	1.3	0.64	6.6 $\pm$ 0.1
J10	c1226	186.75419	33.53426	26.68 $\pm$ 0.05	25.92 $\pm$ 0.06	26.51 $\pm$ 0.11	...	1116 $\pm$ 211	1424 $\pm$ 300	2.3 $\pm$ 0.1	1.3	0.26	7.3 $\pm$ 0.1
J11	m0329	52.43664	-2.20187	26.28 $\pm$ 0.09	25.64 $\pm$ 0.06	26.23 $\pm$ 0.09	1218 $\pm$ 339	946 $\pm$ 245	1041 $\pm$ 296	2.5 $\pm$ 0.1	2.8	0.77	6.9 $\pm$ 0.2
J12	m0329	52.42710	-2.20908	26.39 $\pm$ 0.09	25.70 $\pm$ 0.06	26.75 $\pm$ 0.12	1720 $\pm$ 393	1401 $\pm$ 297	1522 $\pm$ 352	2.0 $\pm$ 0.1	2.9	0.28	6.7 $\pm$ 0.1
J13	m0416	64.04457	-24.07828	24.65 $\pm$ 0.04	23.83 $\pm$ 0.02	24.53 $\pm$ 0.04	801 $\pm$ 127	1198 $\pm$ 110	1052 $\pm$ 126	1.7 $\pm$ 0.1	2.0	0.25	7.7 $\pm$ 0.1
J14	m0416	64.04506	-24.08220	26.51 $\pm$ 0.11	25.58 $\pm$ 0.06	26.35 $\pm$ 0.11	1569 $\pm$ 417	1398 $\pm$ 327	1252 $\pm$ 368	1.7 $\pm$ 0.3	1.4	0.27	7.1 $\pm$ 0.1
J15	m0429	67.39312	-2.88310	24.52 $\pm$ 0.03	23.68 $\pm$ 0.02	24.40 $\pm$ 0.03	1560 $\pm$ 122	1268 $\pm$ 98	1495 $\pm$ 119	2.0 $\pm$ 0.1	2.4	0.72	7.6 $\pm$ 0.1
J16	m0647	101.89789	70.24444	26.75 $\pm$ 0.06	25.97 $\pm$ 0.06	26.79 $\pm$ 0.13	...	1413 $\pm$ 259	1428 $\pm$ 342	1.9 $\pm$ 0.2	1.6	0.40	6.7 $\pm$ 0.1
J17	m0717	109.36207	37.74810	26.41 $\pm$ 0.06	25.70 $\pm$ 0.09	26.76 $\pm$ 0.12	1652 $\pm$ 350	1356 $\pm$ 312	1309 $\pm$ 279	2.4 $\pm$ 0.1	2.1	0.30	6.8 $\pm$ 0.1
J18	m0744	116.22197	39.44121	27.13 $\pm$ 0.12	25.95 $\pm$ 0.08	26.79 $\pm$ 0.14	1630 $\pm$ 554	2056 $\pm$ 501	1203 $\pm$ 444	2.8 $\pm$ 0.2	1.2	0.88	6.6 $\pm$ 0.1
J19	m1115	168.97679	1.51242	27.48 $\pm$ 0.18	26.43 $\pm$ 0.09	27.65 $\pm$ 0.21	1873 $\pm$ 767	2108 $\pm$ 668	2394 $\pm$ 814	2.1 $\pm$ 0.3	1.4	0.24	6.5 $\pm$ 0.1
J20	m1115	168.97415	1.50723	26.56 $\pm$ 0.10	25.70 $\pm$ 0.06	26.96 $\pm$ 0.15	1849 $\pm$ 463	1856 $\pm$ 388	2022 $\pm$ 462	2.4 $\pm$ 0.2	1.7	0.24	6.7 $\pm$ 0.1
J21	m1115	168.95223	1.50104	25.38 $\pm$ 0.05	24.70 $\pm$ 0.04	25.31 $\pm$ 0.05	1072 $\pm$ 166	972 $\pm$ 132	944 $\pm$ 158	2.3 $\pm$ 0.1	2.0	0.39	7.8 $\pm$ 0.1
J22	m1149	177.39721	22.40619	25.59 $\pm$ 0.06	24.51 $\pm$ 0.03	25.80 $\pm$ 0.08	2516 $\pm$ 293	2214 $\pm$ 245	2174 $\pm$ 276	2.1 $\pm$ 0.1	8.4	0.31	6.2 $\pm$ 0.1
J23	m1206	181.55219	-8.78764	26.62 $\pm$ 0.12	25.54 $\pm$ 0.05	26.45 $\pm$ 0.11	1390 $\pm$ 381	1823 $\pm$ 358	1264 $\pm$ 369	2.2 $\pm$ 0.2	1.8	0.40	6.8 $\pm$ 0.1
J24	m1206	181.56703	-8.81022	26.47 $\pm$ 0.08	25.88 $\pm$ 0.06	27.34 $\pm$ 0.26	...	1299 $\pm$ 302	1634 $\pm$ 423	2.2 $\pm$ 0.1	2.7	0.31	6.7 $\pm$ 0.1
J25	m1311	197.74210	-3.16371	25.55 $\pm$ 0.05	24.71 $\pm$ 0.03	25.23 $\pm$ 0.06	...	1161 $\pm$ 150	1233 $\pm$ 195	2.0 $\pm$ 0.1	1.2	0.25	7.5 $\pm$ 0.1
J26	m1311	197.77449	-3.16473	27.19 $\pm$ 0.15	26.22 $\pm$ 0.09	26.91 $\pm$ 0.19	...	1461 $\pm$ 493	1786 $\pm$ 656	2.3 $\pm$ 0.2	1.2	0.28	6.9 $\pm$ 0.2
J27	m1311	197.77126	-3.16271	26.02 $\pm$ 0.08	25.25 $\pm$ 0.06	25.91 $\pm$ 0.12	...	1133 $\pm$ 250	1185 $\pm$ 320	2.6 $\pm$ 0.1	1.3	0.45	7.3 $\pm$ 0.2
J28	m1423	215.95701	24.09266	26.52 $\pm$ 0.06	25.76 $\pm$ 0.06	27.00 $\pm$ 0.15	846 $\pm$ 299	1442 $\pm$ 275	1257 $\pm$ 308	2.0 $\pm$ 0.1	2.2	0.57	6.8 $\pm$ 0.2
J29 <sup>a</sup>	m1720	260.05902	35.62797	27.08 $\pm$ 0.11	25.65 $\pm$ 0.04	27.06 $\pm$ 0.18	...	3145 $\pm$ 555	3648 $\pm$ 718	2.0 $\pm$ 0.2	1.1	0.25	6.6 $\pm$ 0.1
J30	m1720	260.07253	35.62020	27.35 $\pm$ 0.14	26.18 $\pm$ 0.07	27.32 $\pm$ 0.17	1209 $\pm$ 501	2207 $\pm$ 536	2191 $\pm$ 528	2.2 $\pm$ 0.2	2.1	0.23	6.9 $\pm$ 0.1
J31	m1931	292.93714	-26.58000	27.30 $\pm$ 0.17	26.50 $\pm$ 0.10	27.50 $\pm$ 0.19	1974 $\pm$ 710	1524 $\pm$ 544	1266 $\pm$ 589	2.3 $\pm$ 0.3	1.2	0.31	7.0 $\pm$ 0.2
J32	m2129	322.36038	-7.67390	25.98 $\pm$ 0.06	25.16 $\pm$ 0.05	25.69 $\pm$ 0.06	1454 $\pm$ 248	1162 $\pm$ 197	1274 $\pm$ 230	2.1 $\pm$ 0.1	1.2	0.29	7.5 $\pm$ 0.1
J33	m2129	322.36494	-7.70077	27.10 $\pm$ 0.11	26.33 $\pm$ 0.09	27.11 $\pm$ 0.14	1121 $\pm$ 450	1271 $\pm$ 381	1239 $\pm$ 433	2.0 $\pm$ 0.2	1.4	0.46	7.1 $\pm$ 0.2
J34	m2129	322.37282	-7.70210	26.74 $\pm$ 0.08	26.07 $\pm$ 0.12	27.42 $\pm$ 0.23	1059 $\pm$ 376	1386 $\pm$ 433	1611 $\pm$ 500	2.4 $\pm$ 0.1	1.3	0.30	7.1 $\pm$ 0.2
J35	m2137	325.06561	-23.64302	25.73 $\pm$ 0.06	25.06 $\pm$ 0.04	25.87 $\pm$ 0.06	1339 $\pm$ 209	1166 $\pm$ 172	1314 $\pm$ 209	1.4 $\pm$ 0.1	1.6	0.33	7.4 $\pm$ 0.1
J36	m2137	325.04950	-23.67534	25.81 $\pm$ 0.06	25.02 $\pm$ 0.04	25.74 $\pm$ 0.06	862 $\pm$ 190	1180 $\pm$ 174	1242 $\pm$ 207	1.2 $\pm$ 0.1	1.4	0.27	7.7 $\pm$ 0.1
J37	m2137	325.06148	-23.67546	25.64 $\pm$ 0.06	24.95 $\pm$ 0.04	25.53 $\pm$ 0.05	949 $\pm$ 174	942 $\pm$ 146	1020 $\pm$ 177	2.0 $\pm$ 0.1	1.5	0.38	7.9 $\pm$ 0.1
J38	r1347	206.90479	-11.75055	23.73 $\pm$ 0.04	22.97 $\pm$ 0.01	23.60 $\pm$ 0.01	800 $\pm$ 49	826 $\pm$ 44	912 $\pm$ 49	1.8 $\pm$ 0.1	1.4	0.56	8.5 $\pm$ 0.1
J39	r1532	233.22674	30.33152	26.79 $\pm$ 0.14	25.87 $\pm$ 0.08	26.55 $\pm$ 0.12	1127 $\pm$ 440	1265 $\pm$ 372	1243 $\pm$ 436	2.1 $\pm$ 0.2	1.4	0.45	7.2 $\pm$ 0.2
J40	r2248	342.17207	-44.51618	25.80 $\pm$ 0.04	24.93 $\pm$ 0.03	25.90 $\pm$ 0.06	1615 $\pm$ 192	1467 $\pm$ 164	1861 $\pm$ 207	1.8 $\pm$ 0.1	1.6	0.59	7.2 $\pm$ 0.1

**Note.** — (1) identification for each EELG. (2) the short names of cluster fields for each EELG: a1423, Abell 1423; a209, Abell 209; a383, Abell 383; a611, Abell 611; a2261, Abell 2261; c1226, CLJ1226.9+3332; m0329, MACS0329.7-0211; m0416, MACS0416.1-2403; m0429, MACS0429.6-0253; m0647, MACS0647.8+7015; m0717, MACS0717.5+3745; m0744, MACS0744.9+3927; m1115, MACS1115.9+0129; m1149, MACS1149.6+2223; m1206, MACS1206.2-0847; m1311, MACS1311.0-0310; m1423, MACS1423.8+2404; m1720, MACS1720.3+3536; m1931, MACS1931.8-2635; m2129, MACS2129.4-0741; m2137, MS2137-2353; r1347, RXJ1347.5-1145; r1532, RXJ1532.9+3021; r2129, RXJ2129.7+0005; r2248, RXJ2248.7-4431. (3)-(4) coordinates in J2000. (5)-(7) apparent magnitudes for  $I_{814}$ ,  $J_{125}$ ,  $H_{160}$ . (8)-(10) EWs derived from the flux excesses in  $YJ_{110}$ ,  $J_{125}$  and  $JH_{140}$ . (11) continuous slopes inferred from linear fits to the ACS/WFC bands. (12) magnifications estimated from the lensing models. (13) the apparent sizes in  $J_{125}$  images derived from SExtractor in unit of arcsec. (14) stellar masses inferred from Starburst99 [Leitherer et al. \(1999\)](#).

<sup>a</sup> EELGs which have error weighted average of EWs higher than 3000  $\text{\AA}$ .



**Table 2**  
EELG in the Y Sample

EELG	Cluster	RA deg	DEC deg	$I_{814}$ AB	$Y_{105}$ AB	$H_{160}$ AB	$EW_{Y_{105}}$ Å	$EW_{Y_{J110}}$ Å	$EW_{J_{125}}$ Å	$\beta$	$\mu$	FWHM arcsec	log(M) $M_{\odot}$
(1)	(2)	(3)	(4)	(5)	(6)	(7)	(8)	(9)	(10)	(11)	(12)	(13)	(14)
Y1	a383	42.00382	-3.53457	26.46 ± 0.08	25.85 ± 0.09	26.51 ± 0.09	1108 ± 332	985 ± 346	843 ± 269	2.1 ± 0.1	1.4	0.37	7.4 ± 0.3
Y2	a383	42.01025	-3.53787	25.68 ± 0.05	24.76 ± 0.04	25.33 ± 0.04	1387 ± 182	1220 ± 194	1310 ± 157	2.2 ± 0.1	2.0	0.28	6.7 ± 0.1
Y3	a383	42.00173	-3.54142	25.08 ± 0.03	24.59 ± 0.03	25.39 ± 0.04	1085 ± 131	1501 ± 156	415 ± 97	1.7 ± 0.1	1.2	0.25	7.3 ± 0.1
Y4	c1226	186.75661	33.54715	26.55 ± 0.06	25.62 ± 0.06	26.17 ± 0.08	1644 ± 290	1797 ± 380	1640 ± 320	1.7 ± 0.2	1.2	0.26	6.4 ± 0.1
Y5	m0329	52.44139	-2.20040	27.10 ± 0.15	26.15 ± 0.08	27.16 ± 0.16	2072 ± 606	1022 ± 674	1340 ± 545	2.0 ± 0.3	1.5	0.38	7.0 ± 0.2
Y6	m0329	52.41057	-2.20123	26.62 ± 0.10	26.00 ± 0.07	26.70 ± 0.11	1173 ± 343	1217 ± 454	695 ± 313	2.4 ± 0.2	1.6	0.43	6.4 ± 0.3
Y7	m0717	109.40992	37.76028	26.10 ± 0.04	25.45 ± 0.06	26.66 ± 0.15	1399 ± 264	1897 ± 349	...	1.7 ± 0.1	1.8	0.25	6.5 ± 0.1
Y8 <sup>a</sup>	m1115	168.97197	1.51001	27.89 ± 0.26	26.96 ± 0.13	27.80 ± 0.25	1754 ± 910	1626 ± 1226	230 ± 746	...	1.5	0.42	6.3 ± 0.7
Y9 <sup>a</sup>	m1720	260.08484	35.60698	28.24 ± 0.28	26.81 ± 0.11	27.96 ± 0.26	3307 ± 1293	3165 ± 1459	2059 ± 1099	...	1.2	0.45	6.1 ± 0.1
Y10	m2129	322.35663	-7.68367	26.85 ± 0.10	25.93 ± 0.07	26.59 ± 0.09	1562 ± 373	1598 ± 472	1778 ± 404	2.9 ± 0.2	1.5	0.28	7.0 ± 0.1
Y11	m2129	322.33898	-7.69112	23.67 ± 0.01	23.13 ± 0.02	24.19 ± 0.04	1101 ± 63	...	375 ± 51	1.8 ± 0.1	1.5	0.54	8.0 ± 0.1
Y12	r1347	206.87554	-11.74331	26.69 ± 0.07	26.06 ± 0.08	27.01 ± 0.10	1434 ± 343	1647 ± 349	1211 ± 356	2.2 ± 0.1	3.4	0.33	6.2 ± 0.1

**Note.** — As Table 1. But the (5)-(7) are apparent magnitudes for  $I_{814}$ ,  $Y_{105}$ ,  $H_{160}$  and (8)-(10) are EWs derived from the flux excesses in  $YJ_{110}$ ,  $J_{125}$  and  $JH_{140}$ .

<sup>a</sup> Candidates which can be explained with both redshift 5 – 6 galaxies and strong emission lines. The Y8 and Y9 are selected as MACS1115-0352 and MACS1720-1114 in the  $z \sim 6$  catalog of Bradley et al. (2013).